OPEN ACCESS



Skeletal Kinetics Reduction for Astrophysical Reaction Networks

A. G. Nouri , Y. Liu , P. Givi , H. Babaee , and D. Livescu . Department of Mechanical Engineering and Materials Science, University of Pittsburgh, Pittsburgh, PA 15261, USA Laboratory, Los Alamos, NM 87544, USA

*Received 2023 May 10; revised 2024 April 25; accepted 2024 April 28; published 2024 May 29

Abstract

A novel methodology is developed to extract accurate skeletal reaction models for nuclear combustion. Local sensitivities of isotope mass fractions with respect to reaction rates are modeled based on the forced optimally time-dependent (f-OTD) scheme. These sensitivities are then analyzed temporally to generate skeletal models. The methodology is demonstrated by conducting skeletal reduction of constant density and temperature burning of carbon and oxygen relevant to Type Ia supernovae (SNe Ia). The 495-isotopes Torch model is chosen as the detailed reaction network. A map of maximum production of 56 Ni in SNe Ia is produced for different temperatures, densities, and proton-to-neutron ratios. The f-OTD simulations and the sensitivity analyses are then performed with initial conditions from this map. A series of skeletal models are derived and their performances are assessed by comparison against currently existing skeletal models. Previous models have been constructed intuitively by assuming the dominance of α -chain reactions. The comparison of the newly generated skeletal models against previous models is based on the predicted energy release and 44 Ti and 56 Ni abundances by each model. The consequences of $\gamma_e \neq 0.5$ in the initial composition are also explored where γ_e is the electron fraction. The simulated results show that 56 Ni production decreases by decreasing γ_e as expected, and that the 43 Sc is a key isotope in proton and neutron channels toward 56 Ni production. It is shown that an f-OTD skeletal model with 150 isotopes can accurately predict the 56 Ni abundance in SNe Ia for $\gamma_e \lesssim 0.5$ initial conditions.

Unified Astronomy Thesaurus concepts: Stellar nucleosynthesis (1616); Reaction rate equations (2239); Stellar physics (1621); Astrophysical fluid dynamics (101); Nuclear astrophysics (1129)

1. Introduction

Direct implementation of detailed reaction networks (RNs) containing many isotopes and reactions in hydrodynamic flow solvers is computationally very expensive. In most cases, it is unavoidable to use efficient reaction kinetics models to conduct large-scale hydrodynamic simulations pertaining to astrophysical explosions, such as Type Ia supernovae (SNe Ia). These reaction kinetics models, which are usually extracted from detailed reaction networks, should reasonably estimate the released energy and isotope abundances. Integration of the ordinary differential equations representing the abundance levels of a set of isotopes of reacting nuclei in the continuum limit serves two functions in stellar models. The primary function of hydrodynamics is to provide the magnitude and sign of the nuclear energy generation rate (Weaver et al. 1978; Bravo et al. 2019; Arnould & Goriely 2020). This is usually the largest energy source in regions conducive to nuclear reactions, and its accurate determination is essential for stellar models. These models usually require accurate predictions of the energy generated by nuclear burning over a wide range of temperatures, densities, and compositions (Timmes 1999; Timmes et al. 2000; Röpke & Sim 2018). The other function is to describe the evolution of the composition. In some stellar events, the isotopic abundances themselves are of primary interest for understanding the origin and evolution of the chemical elements (Pagel 2009; Matteucci 2012; Kobayashi et al. 2020). Moreover, matching observational evidence of certain isotopes, e.g., ⁵⁶Ni in SN light curves, gives confidence in the

Original content from this work may be used under the terms of the Creative Commons Attribution 4.0 licence. Any further distribution of this work must maintain attribution to the author(s) and the title of the work, journal citation and DOI.

underlying computational model (Seitenzahl & Townsley 2017; Bora et al. 2022).

Thousands of isotopes can participate in an RN during a stellar phenomenon (Wanajo 2013; Nishimura et al. 2015; Fernández et al. 2017; Lippuner & Roberts 2017; Psaltis et al. 2022). Accurate predictions of the nuclear energy generation rate and the composition changes in such RNs is computationally expensive. The largest block of memory in a stellar model is usually used for storing the isotopic abundances of every computational cell at all time steps. Even with modern methods for solving stiff systems of ordinary differential equations (ODEs), integration of the evolution equations of the isotopic abundances dominates the total cost of a stellar model when the number of isotopes evolved is $\mathcal{O}(100)$ (Arnett 1996; Nouri et al. 2019). To decrease the computational cost, one has to make a choice between having fewer isotopes (order reduction) or less spatial resolution (or mass resolution). The general response to this trade-off has been the order reduction by using simplified RNs within hydrodynamic solvers to calculate an approximate energy generation rate and isotope mass fractions during stellar explosions (Röpke & Sim 2018). As a postprocessing step, the detailed nuclear composition of the ejecta is computed using a large RN by employing Lagrangian tracer particles (Thielemann et al. 1986; Townsley et al. 2016; Leung & Nomoto 2018; Bravo et al. 2019; Seitenzahl & Pakmor 2023). These particles represent passive mass elements and can be evolved in situ, within the simulation, with time steps dictated by the hydrodynamic solvers, or off-site, using an additional reconstruction step based on the snapshot data (Sieverding et al. 2023). Current large simulations can use at least 10⁶ tracer particles to calculate detailed 3D spatial composition (Seitenzahl & Pakmor 2023).

Order reduction techniques for nuclear reaction networks require extensive experience and expertize. For example, common α -chain RNs (with 13/19/21 isotopes; Paxton et al. 2011, 2015) contain a minimal set of nuclei to approximate the energy generation rate for stellar simulations of SNe Ia (Paxton et al. 2011). These RNs are optimized by decades of shared knowledge (Yoshida et al. 2021). Order reduction techniques for nuclear RNs also include explicit asymptotic (Guidry et al. 2013), quasi-steady-state (Mott et al. 2000; Guidry & Harris 2013), and quasi-equilibrium (Bodansky et al. 1968; Woosley et al. 1973; Khokhlov 1981; Hix et al. 1998, 2007; Meyer et al. 1998; Timmes et al. 2000; Kushnir & Katz 2020) methods. However, these RNs, while fast and lightweight, are rigid with respect to adding or removing isotopes (Paxton et al. 2011).

In chemical combustion, recent advances in data-driven techniques and sensitivity analysis have opened the possibility of significantly enhancing the efficiency and flexibility of generating reduced RNs (Lu & Law 2009). Recent skeletal models, i.e., optimized subsets of detailed reaction networks, can be prepared in an optimized and automated manner, with consistent accuracy throughout the evolution of the network, and can be adapted based on the availability of computing resources. Utilizing such capabilities for nuclear combustion can address certain issues regarding the model reduction of nuclear RNs, e.g., scenarios where the experience required to generate quality reduced models might be lacking. There is a history of utilizing sensitivity analysis in nuclear combustion. This includes studies of the Big Bang (Beaudet & Reeves 1983; Delbourgo-Salvador et al. 1985; Krauss & Romanelli 1990; Smith et al. 1993; Nollett & Burles 2000; Cyburt 2004), stellar explosions (Hix et al. 2003; Parikh et al. 2008; Longland et al. 2010; Bravo & Martinez-Pinedo 2012; Longland 2012; Bliss et al. 2020), and the *r*-process (Mumpower et al. 2012, 2015; Sprouse et al. 2020; Barnes et al. 2021). Most of these contributions are based on direct Monte Carlo simulations and their focus is on understanding the impact of nuclear reaction rate and/or other nuclear uncertainties on the resulting nucleosynthesis predictions.

The goal of this work is to develop skeletal RNs suitable for situations pertaining to SNe Ia. A skeletal model is a subset of a detailed reaction model which is generated by eliminating unimportant isotopes and reactions (Smooke 1991; Peters & Rogg 1993; Stagni et al. 2016; Li et al. 2020). The skeletal reduction is usually the first step in developing a model reduction. The next steps in the reduction include timescale analysis techniques, e.g., quasi-steady-state approximation (Stiefenhofer 1998; Girimaji & Ibrahim 2014), partial equilibrium approximation (Rein 1992; Goussis 2012), and ratecontrolled constrained equilibrium (Keck 1990; Hadi et al. 2016) among others. To develop skeletal RNs for SNe Ia, first local sensitivities of isotope mass fractions with respect to reaction rates are analyzed during the constant density and temperature (constant- ρT) burning of carbon and oxygen with different initial conditions. The isotopes are ranked based on their sensitivities (importance), and several sets of skeletal models with different levels of accuracy are generated by selecting different numbers of important isotopes. The sensitivities are computed by the forced optimally timedependent (f-OTD) methodology (Donello et al. 2022). This is an on-the-fly reduced-order modeling (ROM) technique, recently introduced for computing sensitivities in evolutionary dynamical systems. Unlike the traditional ROM techniques, the

f-OTD does not require any offline data generation, and all the computations are carried out online. Nouri et al. (2022) and Liu et al. (2024) conducted a similar sensitivity-based skeletal kinetics reduction technique for chemical combustion, which automatically eliminates unimportant reactions and species. Time-dependent f-OTD modes are able to capture sudden transitions associated with the largest finite-time Lyapunov exponents (Babaee et al. 2017b). Time-dependent bases have also been used for stochastic ROM (Sapsis & Lermusiaux 2009; Cheng et al. 2013; Babaee et al. 2017a; Babaee 2019; Patil & Babaee 2020) and on-the-fly ROM of the reacting species transport equation (Ramezanian et al. 2021; Aitzhan et al. 2022). The f-OTD can be formulated as a special case of the dynamical low-rank approximation (Koch & Lubich 2007). The specific objectives here are (i) to introduce the f-OTD technique for computing sensitivities for a nuclear combustion system, and (ii) to find skeletal models for thermonuclear burning in SNe Ia. The first set of skeletal models are applicable to both neutron-rich and equal numbers of neutron and proton scenarios. This is facilitated by the f-OTD skeletal reduction technique, without a priori assumptions or expertize, e.g., the assumption of an equal number of protons and neutrons. Section 2 briefly presents the theory behind the f-OTD method for constant- ρT burning in SNe Ia and the automatic process of eliminating unimportant isotope/reaction from a detailed RN. This elimination process is explained in Section 3 with a simple example, starting from an RN with 21 isotopes and reducing it to a skeletal model with 10 isotopes. Section 4 describes the application of the f-OTD skeletal reduction method to the Torch RN³ (Timmes 1999; Timmes & Swesty 2000; Anninos et al. 2019). This RN considers 495 isotopes, up to ⁹¹Tc, and 6012 reactions. Different skeletal models with different levels of accuracy are extracted and their ability to reproduce the energy release and ⁴⁴Ti and ⁵⁶Ni abundances of the Torch model are analyzed. Section 5 provides the concluding remarks.

2. Skeletal Reduction with f-OTD Method

2.1. Reduced-order Modeling of the Sensitivity Matrix with f-OTD

For the model description, let isotope k have total charge Z_k and atomic weight A_k . Let the aggregate total of isotope k have a mass density ρ_k and a number density n_k in a material with the temperature T and the total mass density ρ . The mass fraction of isotope k is defined as $x_k = \rho_k/\rho = n_k A_k/\rho N_A$ where $N_A = 6.02252 \times 10^{23}$ particles mol⁻¹ (Avogadro's number). The mean atomic weight is $A_m = (\sum x_k/A_k)^{-1}$, and is the equivalent of the mixture molar mass from the combustion literature (Williams 1985). The nuclear abundance of isotope kis $y_k = x_k/A_k = n_k/(\rho N_A)$, the mean charge per isotope is $Z_m = A_m \sum Z_k x_k / A_k$, and the electron abundance, or electron number fraction, is $y_e = Z_m/A_m$. This is related to the neutron excess, η , by $\eta = 1 - 2y_e$, so that $\eta = 0$ corresponds to $y_e = 0.5$. The total scalar pressure, the total specific internal energy, and the total specific entropy are denoted by p_{tot} , e_{tot} , and s_{tot} , respectively (Nouri et al. 2019). Other quantities such as the specific heats or adiabatic indices can be determined via an equation of state (Timmes & Arnett 1999) once the partial derivatives of the pressure and the specific internal energy with

https://cococubed.com/code_pages/net_torch.shtml

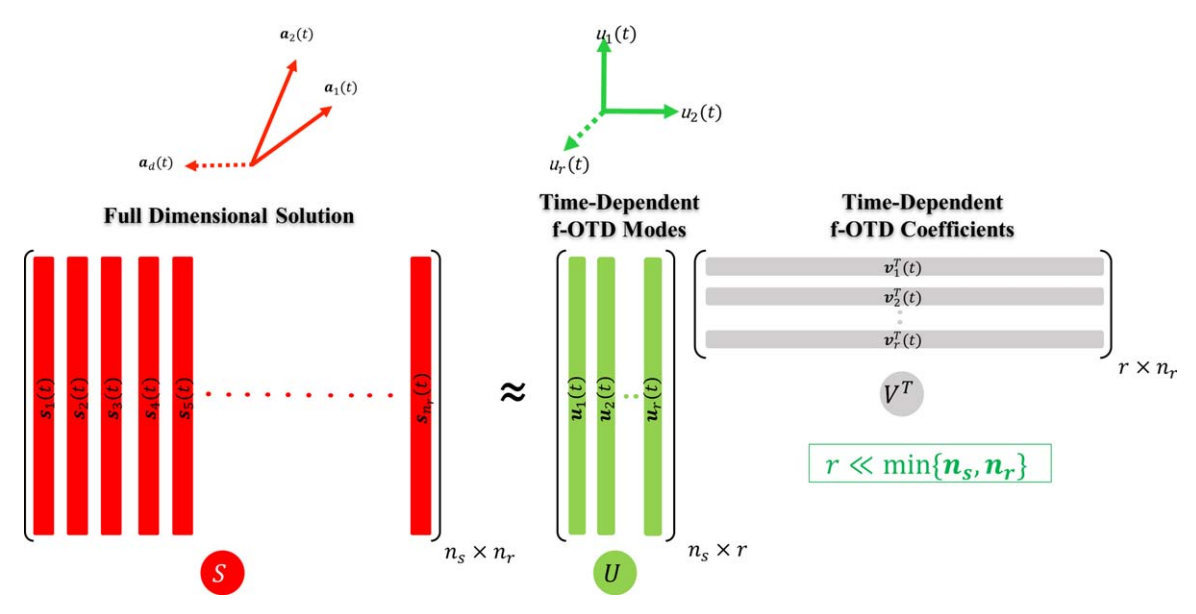


Figure 1. Modeling sensitivity matrix S(t) as a multiplication of two low-ranked matrices U(t) and Y(t) that evolve according Equation (5). Reprinted from Nouri et al. (2022) with permission.

respect to the density and temperature are known. Consider a nuclear system of n_s isotopes reacting through n_r reactions:

$$\sum_{k=1}^{n_s} \nu'_{kj} \mathbb{M}_k \leftrightharpoons \sum_{k=1}^{n_s} \nu''_{kj} \mathbb{M}_k, \ j = 1, \dots n_r, \tag{1}$$

where \mathbb{M}_k is a symbol for isotope k, and ν'_{kj} and ν''_{kj} are the stoichiometric coefficients of isotope k in reaction j. Changes of abundances $y = [y_1, y_2, ..., y_{n_s}]^T$ in constant- ρT burning within a carbon-oxygen white dwarf (WD) with constant temperature and pressure can be described by the following initial value problem (Timmes et al. 2000):

$$\frac{d\mathbf{y}_k}{dt} = f_k(\mathbf{y}, \alpha) = \frac{A_k}{N_A} \sum_{i=1}^{n_r} \nu_{kj} \alpha_j \mathcal{Q}_j, \ \mathbf{y}(0) = \mathbf{y}_0,$$
 (2)

where $t \in [0, t_f]$ is time, t_f is the final time, and $\alpha =$ $[1, 1, ..., 1] \in \mathbb{R}^{n_r}$ is the vector of perturbation parameters. In Equation (2), Q_i is the progress rate of reaction j and is equal to the following for one- and two-body reactions:

$$\nu_{kj} = \nu_{kj}'' - \nu_{kj}',\tag{3a}$$

$$Q_{j} = K_{f,j} \prod_{k=1}^{n_{s}} (n_{k})^{\nu'_{kj}} - K_{r,j} \prod_{k=1}^{n_{s}} (n_{k})^{\nu''_{kj}}$$

$$= K_{f,j} \prod_{k=1}^{n_{s}} (\rho_{Yk} N_{A})^{\nu'_{kj}} - K_{r,j} \prod_{k=1}^{n_{s}} (\rho_{Yk} N_{A})^{\nu''_{kj}}.$$
(3b)

Here, $K_{f,j}$ and $K_{r,j}$ are the forward and reverse rate of reaction j. The quantity $\prod_{k=1}^{n_s} (n_k)^{\nu'_{kj}}$ is the total possible number of elementary reactions per unit volume (obtained by counting the number of possible collisions) and is based on the number density of particles. Because the collision energies are well below the Coulomb barrier, most collisions do not result in nuclear reactions. Thus, the reaction rate is the product of the collision rate and the tunneling probability.

The abundances in Equation (2) are perturbed by infinitesimal variations of α_i , by letting $\alpha_i = 1 + \delta \alpha_i$, where $\delta \alpha_i \ll 1$ for $j = 1, 2, ..., n_r$. The perturbation with respect to α_i amounts to an infinitesimal perturbation of progress rates Q_i . The sensitivity matrix, $S(t) = [s_1(t), s_2(t), ..., s_{n_r}(t)] \in \mathbb{R}^{n_s \times n_r}$, contains local sensitivity coefficients, $s_i = \partial y / \partial \alpha_i$, and can be calculated by solving the sensitivity equation (SE),

$$\frac{dS_{ij}}{dt} = \sum_{m=1}^{n_s} \frac{\partial f_i}{\partial y_m} \frac{\partial y_m}{\partial \alpha_j} + \frac{\partial f_i}{\partial \alpha_j} = \sum_{m=1}^{n_s} L_{im} S_{mj} + F_{ij}, \quad (4)$$

where $L_{im}=rac{\partial f_i}{\partial \mathbf{y}_m}$ and $F_{ij}=rac{\partial f_i}{\partial lpha_j}$ are the Jacobian and the forcing

The model reduction strategy is based on selecting reactions, whose perturbations grow most intensely in the abundance equation (Equation (2)). The selection of important reactions is performed by instantaneous observation of modeled sensitivities. In f-OTD, the sensitivity matrix S(t) is modeled by factorizing it into a time-dependent subspace in the n_s -dimensional phase space of abundances represented by a set of f-OTD modes: $U(t) = [\mathbf{u}_1(t), \mathbf{u}_2(t), ..., \mathbf{u}_r(t)] \in \mathbb{R}^{n_s \times r}$. These modes are orthonormal $\mathbf{u}_{i}^{T}(t)\mathbf{u}_{i}(t) = \delta_{ij}$ at all t, where δ_{ij} is the Kronecker delta. The rank of $S(t) \in \mathbb{R}^{n_s \times n_r}$ is $d = \min\{n_s, n_r\}$ while the f-OTD modes represent a rank-r subspace, where $r \ll d$. To this end, the sensitivity matrix is approximated via the f-OTD decomposition (Figure 1) as $S(t) \approx U(t)V^{T}(t)$ where $V(t) = [\mathbf{v}_1(t), \mathbf{v}_2(t), ..., \mathbf{v}_r(t)] \in \mathbb{R}^{n_r \times r}$ is the f-OTD coefficient matrix. This decomposition is a low-rank approximation of the sensitivity matrix S(t). Therefore, $U(t)V(t)^T$ closely approximates S(t) and it is not exact. Both U(t) and V(t) are time dependent, and their explicit time dependency on t is dropped for brevity. Figure 1 shows the schematic of the decomposition of S into f-OTD components U and V. The evolution equations for U and V are obtained by substituting the sensitivity decomposition $(S(t) \approx U(t)V^{T}(t))$ into Equation (4):

$$\frac{dU}{dt} = QLU + QFVC^{-1},\tag{5a}$$

$$\frac{dV}{dt} = VL_r^T + F^TU, \tag{5b}$$
 where $Q = I - UU^T$ is the orthogonal projection onto the space

spanned by the complement of U and $C = V^T V \in \mathbb{R}^{r \times r}$ is a

correlation matrix. Matrix C(t) is, in general, a full matrix implying that the f-OTD coefficients are correlated. $L_r = U^T L U \in \mathbb{R}^{r \times r}$ is a reduced linearized operator. Equation (5) represents a coupled system of ODEs and constitutes the f-OTD evolution equations. The f-OTD modes align themselves with the most instantaneously sensitive directions of the abundance evolution equation when perturbed by α . It is shown by Babaee et al. (2017b) that when α is the perturbation to the initial condition, the OTD modes converge exponentially to the eigen-directions of the Cauchy–Green tensor associated with the most intense finite-time instabilities.

The primary computational advantage of using f-OTD is that the method only evolves two skinny matrices containing $(n_s + n_r) \times r$ elements as opposed to $n_s \times n_r$ elements in the SE (Equation (4)). This reduces the required memory for ODE solvers drastically and facilitates the application of stiff solvers for evolving sensitivities. Moreover, in the f-OTD decomposition, the sensitivities are stored in the *compressed form*, i.e., matrices U and V are kept in the memory as opposed to their multiplication UV^T , i.e., the *decompressed form*. Therefore, in comparison to the full SE, f-OTD decomposition results in the memory compression ratio of $(n_s \times n_r)/((n_s + n_r)r)$.

2.2. Identification of Important Reactions and Isotopes

In the f-OTD skeletal reduction, modeled sensitivities are computed in a factorized format by solving Equations (2), (5a), and (5b), and the values of U, V, and v are stored at resolved time steps $t_i \in [0, t_f]$. Equation (2) is initialized with different sets of isotope abundances, temperature, and density within their ranges of interest. Each simulation with a different initial condition is identified as a case. At each resolved time step and for each case, the eigen decomposition of $S^TS \in \mathbb{R}^{n_r \times n_r}$ is computed as $A\Lambda A^T$, and the vector $\mathbf{w} = (\Sigma \lambda_i |\mathbf{a}_i|)/(\Sigma \lambda_i) \in \mathbb{R}^{n_r}$ is basically the average of eigenvectors of the $S^{T}S$ matrix weighted based on their associated eigenvalues (λ_i) , and prevents dealing with each eigenvector (a_i) separately. Each component of w, i.e., w_i , is positive and associated with a certain reaction (ith reaction). The larger the w_i value, the more important the reaction i is. The $w_{\max,i}$ denotes the highest value of w_i through all resolved time steps and cases. The elements of the w_{max} vector are sorted in descending order to find the indices of the most important reactions in the detailed model. Isotopes are also sorted based on their first presence in the sorted reactions, i.e., isotopes which first show up in a higherranked reaction would be more important than an isotope which first participates in a lower-ranked reaction. This results in a reaction and isotope ranking based on w_{max} vector. Finally, a set of isotopes are chosen by defining a threshold ϵ on the element of the w_{max} vector and eliminating isotopes whose associated $w_{\max,i}$ are less than ϵ . This terminates reactions which include the eliminated isotopes from the detailed model. Since the model reduction is reaction based, any nonreactive isotope with a nonzero mass fraction in the initial condition must be manually added to the skeletal model.

In summary, the nuclear combustion system is instantaneously observed, and the reactions are sorted based on their effects on sensitivities to find the most important isotopes. These isotopes and the reactions which connect them together create the skeletal models. In combustion systems, perturbations with respect to "fast" reactions generate very

large sensitivities for short time periods which vanish as $t \to \infty$. On the other hand, perturbations with respect to "slow" reactions generate smaller and more sustained sensitivities. The approach here is based on the instantaneous observation of sensitivities; both slow and fast reactions can leave an imprint on the instantaneous normalized reaction vector (w) if their imprints are larger than the threshold value (ϵ) . However, if the sensitivities associated with fast and slow reactions from predetermined times and locations are combined with each other before dimension reduction, as commonly done in principal component analysis type schemes, the smaller sensitivities associated with slow reactions would be outweighed by the large sensitivities associated with fast reactions.

3. Skeletal Reduction on the Approx21 RN

The process of eliminating unimportant reactions and isotopes from a kinetics model with f-OTD is demonstrated in this section with a simple example. Let us start with the Approx21 model, which is the default MESA network (Paxton et al. 2011, 2015) for alpha chain reactions. Approx21 evolves $n_s = 21$ isotopes: n, p, 1 H, 3 He, 4 He, 12 C, 14 N, 16 O, 20 Ne, 24 Mg, 28 Si, 32 S, 36 Ar, 40 Ca, 44 Ti, 48 Cr, 56 Cr, 52 Fe, 54 Fe, 56 Fe, and 56 Ni through $n_r = 112$ reactions. In this RN, $(\alpha, p)(p, \gamma)$ and $(\gamma, p)(p, \gamma)$ α) links are included in order to obtain reasonably accurate energy generation rates and abundance levels when the temperature exceeds 2.5×10^9 K. At these elevated temperatures, the flows through the $(\alpha,p)(p,\gamma)$ sequences are faster than the flows through the (α, γ) channels. An $(\alpha, p)(p, \gamma)$ sequence is, effectively, an (α, γ) reaction through an intermediate isotope. By assuming steady-state proton flows through intermediate isotopes ²⁷Al, ³¹P, ³⁵Cl, ³⁹K, ⁴³Sc, ⁴⁷V, ⁵¹Mn, and ⁵⁵Co, this strategy avoids explicitly evolving the abundances of the proton or intermediate isotopes.⁴ The skeletal reduction is exemplified here by analyzing only one case for the constant- ρT burning of a mixture of carbon and oxygen in a WD progenitor.

The ignition initiates with $T_9 = 3$, $\rho_9 = 1$, and $\mathbf{x}_{C,0} = \mathbf{x}_{O,0} = 0.5$, so $\mathbf{y}_e = 0.5$. Here, $T_9 \equiv T/(10^9 \, \mathrm{K})$ and $\rho_9 \equiv \rho/(10^9 \, \mathrm{g \ cm}^{-3})$. The sensitivities evolve in two phases. In the first, the full-dimensional SE (Equation (4)) is solved for a very small time period, e.g., until $t = 10^{-12} \, \mathrm{s}$, to generate the initial conditions for the f-OTD simulation. In the second phase, the sensitivity matrix (*S*) is approximated by evolving the f-OTD equations (Equation (5)). The *U* and *Y* matrices are initialized by eigenvalue decomposition of the full sensitivity matrix (*S*) at the end of the first phase. Figure 2 shows the evolution of the eigenvalues of the S^{TS} matrix. It is indicated that (i) λ_1 is an order of magnitude larger than λ_2 most of the time, and (ii) the modeled sensitivities converge by adding more modes. Therefore, f-OTD simulation with r = 1 provides a reasonable estimation of sensitivities, which is enough if the final goal is to determine the importance of reactions/isotopes.

Figure 3 shows the ranking of reactions and isotopes in Approx21 associated with the constant- ρT burning case. It is apparent that reactions 4 ($^{12}\text{C}(^{12}\text{C},\alpha)^{20}\text{Ne}$), equilibrium reactions 92 ($^{24}\text{Mg}(\alpha,p)^{27}\text{Al}(p,\gamma)^{28}\text{Si}$), 93 ($^{28}\text{Si}(\alpha,p)^{31}\text{P}(p,\gamma)^{32}\text{S}$), and 95 ($^{36}\text{Ar}(\alpha,p)^{39}\text{K}(p,\gamma)^{40}\text{Ca}$), and reaction 6 ($^{16}\text{O}(^{16}\text{O},\alpha)^{28}\text{Si}$) are the first five most important reactions, and isotopes ^{4}He , ^{12}C , ^{20}Ne , ^{24}Mg , and ^{28}Si are the first five most important isotopes in Approx21 for the ignition case considered.

⁴ https://cococubed.com/code_pages/burn_helium.shtml

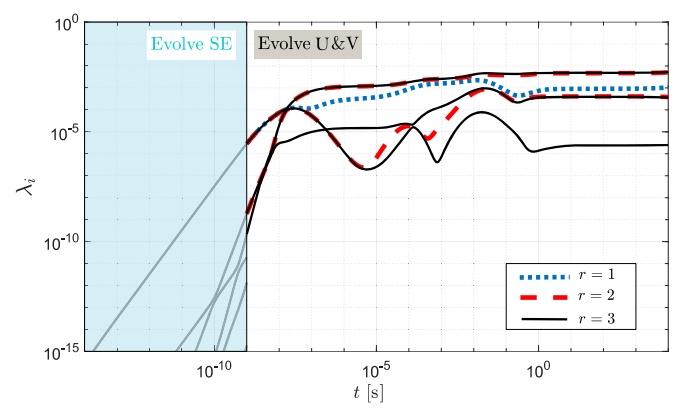


Figure 2. Model reduction for Approx21: eigenvalues of the $S^{\rm TS}$ matrix. The sensitivity matrix, S, initially evolves exactly via the SE (Equation (4)), and then evolves approximately with the f-OTD equations (Equation (5)). The f-OTD simulation $(t > 10^{-9})$ only evolves r modes of the full-order model $(t < 10^{-9})$. Ignition data is gathered from the constant- ρT burning simulation case described in Figure 3.

The f-OTD-10 model is then created based on the algorithm described in Section 2.2 and contains 10 most important isotopes shown in Figure 3, i.e., 4 He, 12 C, 20 Ne, 24 Mg, 28 Si, 32 S, 36 Ar, 40 Ca, 16 O, and 44 Ti. Approx13 (Timmes et al. 2000) is a 13 isotope (4 He, 12 C, 16 O, 20 Ne, 23 Mg, 28 Si, 32 S, 36 Ar, 40 Ca, 44 Ti, 48 Cr, 52 Fe, and 56 Ni) reaction network which is also extracted from Approx21 but over a wider time range to produce 56 Ni. That is why Approx13 contains three more isotopes, i.e., 48 Cr, 52 Fe, and 56 Ni in comparison with f-OTD-10. Nevertheless, this simple exercise demonstrates the ability of f-OTD methodology to extract the relevant isotopes for a given set of conditions and starting RN. Figure 4 demonstrates the performance of f-OTD-10 RN in predicting the evolution of isotope mass fractions over its design conditions ($T_9 = 3$, $\rho_9 = 1$, $x_{C,0} = x_{O,0} = 0.5$, and $t \in [0, 10^4]$ s).

4. Skeletal Reduction on the Torch RN

In SNe Ia, the carbon and oxygen burn together to produce nuclei from silicon to the iron peak that are being ejected into the interstellar medium (Nomoto 1997; Woosley et al. 2002; Lippuner & Roberts 2017; Johnson 2019). As this type of SN does not produce a significant amount of free neutrons, it does not synthesize elements beyond the iron peak (Johnson 2019). Nevertheless, some heavier isotopes can contribute to reactions involving isotopes important to light-curve observations, such as ⁵⁶Ni. The 495-isotope version of the Torch RN (Paxton et al. 2015) is chosen to represent the detailed RN in this section. The Torch RN extends from ¹H to ⁹¹Tc (Timmes 1999) with $n_s = 495$ and $n_r = 6012$. The weak reactions are turned on, and no screening is performed on the reaction rates (Fuller et al. 1985). The Helmholtz equation of state as developed by Timmes & Swesty (2000) is used with Coulomb correction to calculate the internal energy and the pressure. Several skeletal RNs have been previously proposed based on the Torch model for inline calculations (Timmes 1999; Timmes & Swesty 2000; Anninos et al. 2019) and are used in the MESA code (Paxton et al. 2011, 2015; Anninos et al. 2019). These include a bare minimum model of the α -chain reactions using 13 isotopes, a 19-isotope RN to also accommodate some hydrogen burning (Weaver et al. 1978), and a 21-isotope RN that adds ⁵⁶Cr and ⁵⁶Fe and respective equilibrium reaction sequences to the

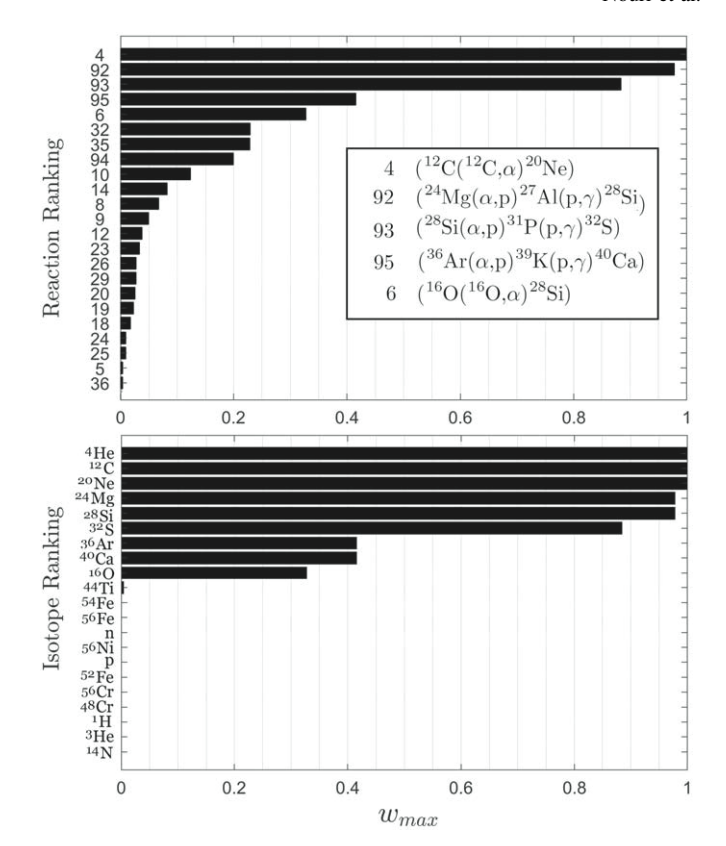


Figure 3. Model reduction for Approx21: reaction and isotope ranking based on their associated w_{max} from one constant- ρT burning simulation case with $T_9 = 3$, $\rho_9 = 3$, and initial composition of $x_{\text{C},0} = x_{\text{C},0} = 0.5$ with $y_{e,0} = 0.5$.

19-isotope network to attain a lower y_e value for pre-SN models (Paxton et al. 2015). Several important isotopes are produced in burning scenarios with y_e significantly lower than 0.5. For example, Woosley (1997) suggests that ⁴⁸Ca can only be produced in nature in a subset of SNe Ia, with y_e in the range 0.41–0.42 and high burning density. The Torch RN covers such scenarios. On the other hand, the performances of the existing skeletal models have not been systematically examined to cover both $y_e = 0.5$ and $y_e < 0.5$ scenarios. This is addressed here by considering initial conditions with different y_e values and choosing the 21-isotope RN skeletal model (hereafter denoted Approx21) for comparison with the proposed skeletal RNs.

The SNe Ia progenitor population and burning scenarios cover a wide range of temperatures and densities (Hillebrandt & Niemeyer 2000) so that, most likely, a single skeletal model with a limited number of isotopes (n_s) cannot yield accurate predictions over the full range of conditions that would be covered by a detailed RN. Because of the importance of ⁵⁶Ni in SNe Ia, the skeletal models in this work are designed to predict the evolution of x56Ni correctly. For this purpose, a map of maximum production of this isotope is produced during the course of constant- ρT burning in SNe Ia as shown in Figure 5. The Torch RN is run 10,000 times on a 100×100 grid of T_9 and ρ_9 for $y_{e,0}$ values of 0.4955 and 0.5. It is observed that ⁵⁶Ni is only significantly produced within certain ranges of the temperature and the density values, with a noticeable shift of the ⁵⁶Ni production near the peak. In particular, the peak occurs around $T_9 = 4.0$ at lower densities. Moreover, the maximum production of 56 Ni is decreased by decreasing $y_{e,0}$

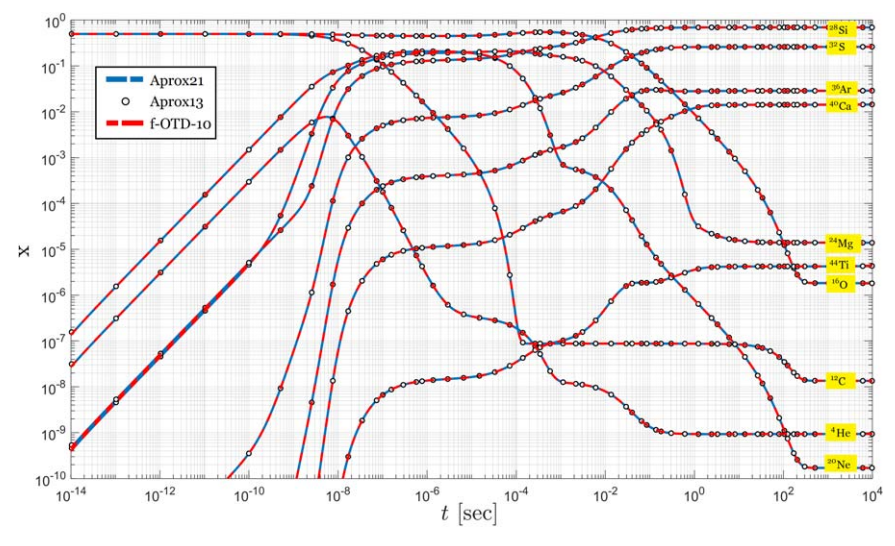


Figure 4. Model reduction for Approx21: evolution of isotope mass fractions based on Approx21, Approx13, and f-OTD-10. The last two models are generated from Approx21.

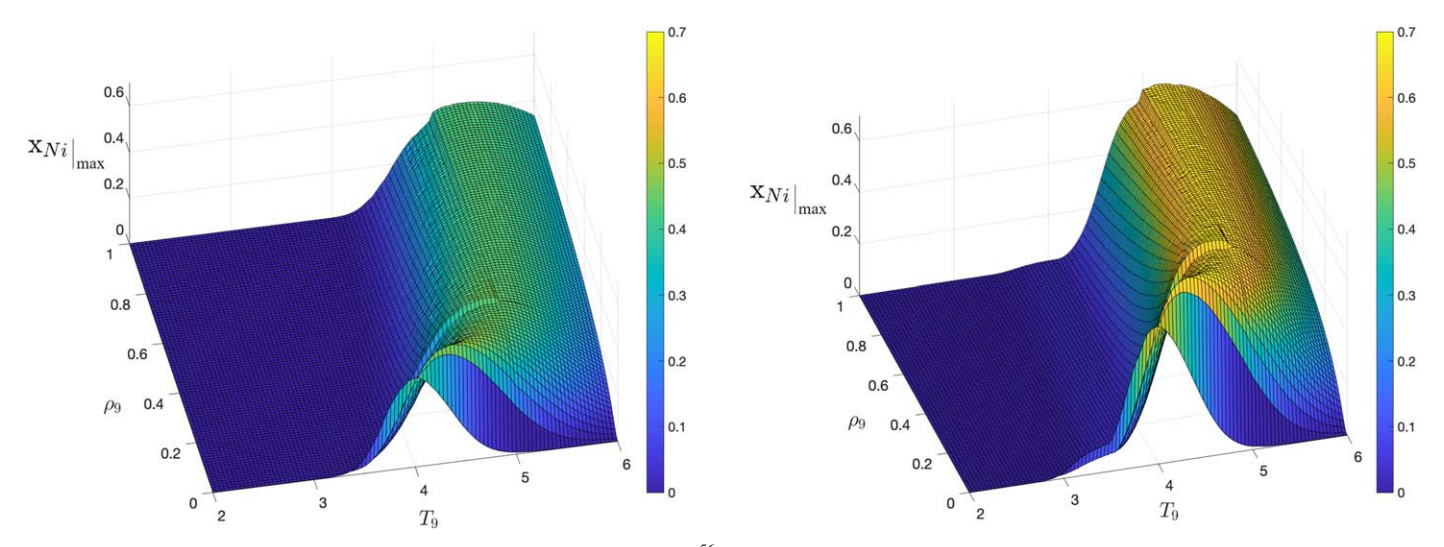


Figure 5. Maximum mass fraction of 56 Ni during constant- ρT burning of SNe Ia.

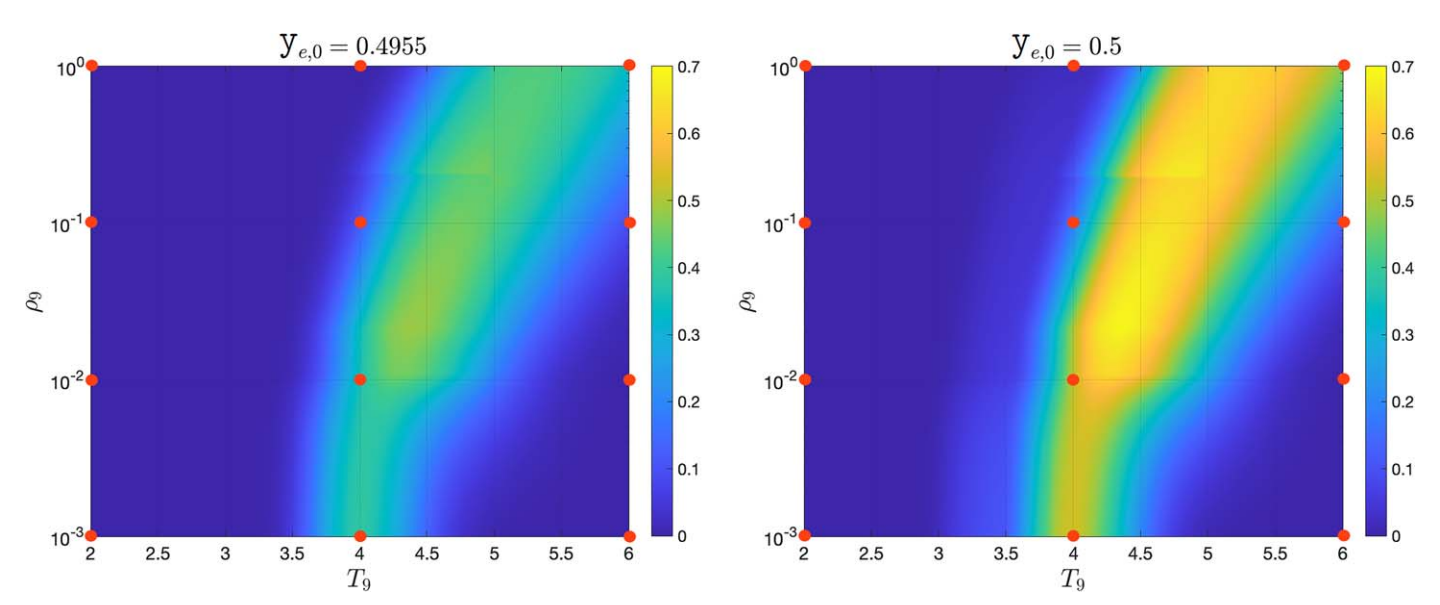


Figure 6. 2-D version of Figure 5, to highlight the f-OTD cases (red circles).

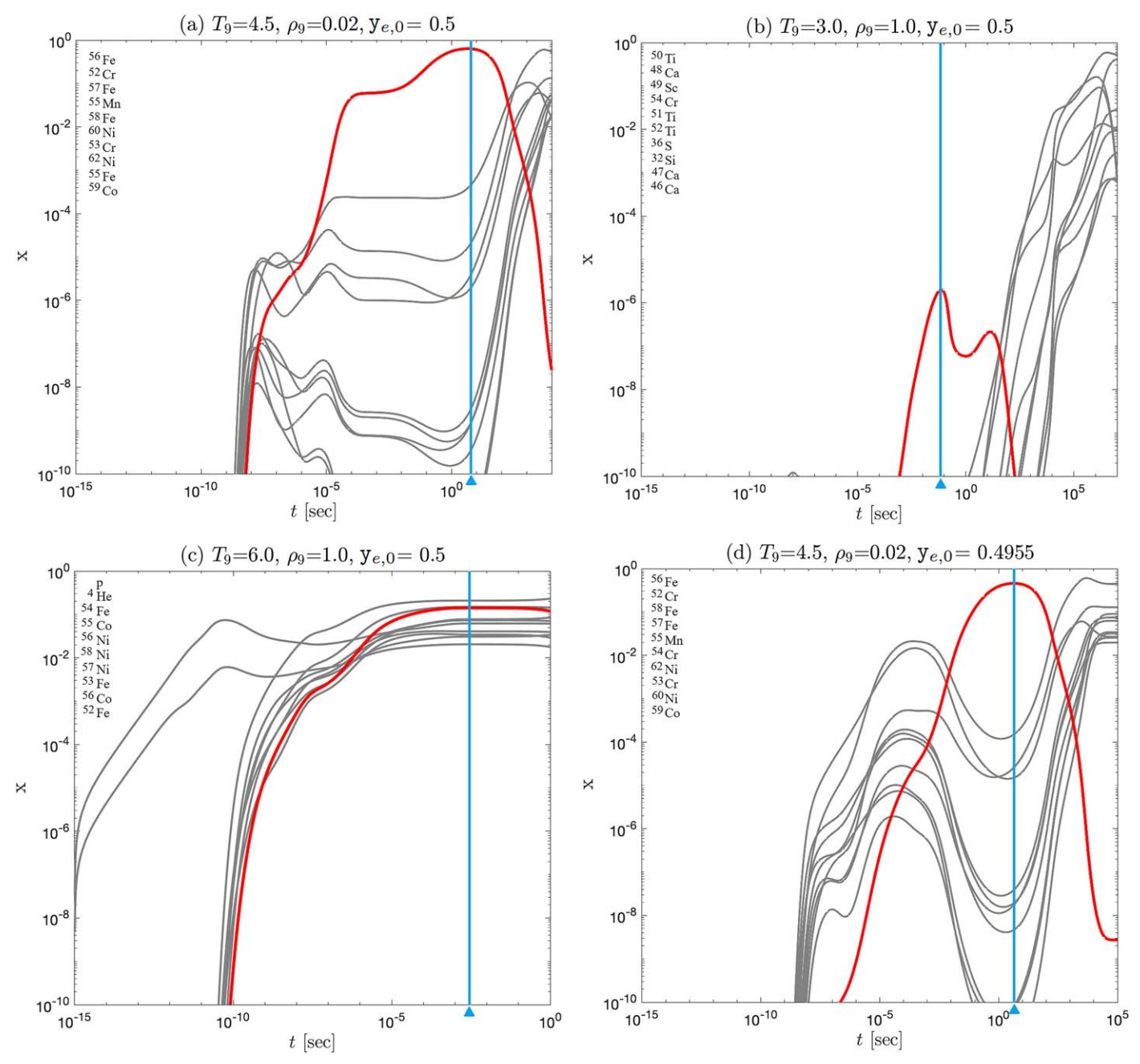


Figure 7. Evolution of isotope mass fractions in Torch with different initial conditions, highlighting different scenarios for ⁵⁶Ni evolution. The blue lines indicate the final time of the f-OTD simulations and sensitivity analysis. The red and gray lines represent the ⁵⁶Ni mass fraction and the 10 isotopes with the highest final mass fractions observed during the portrayed ignition process. These isotopes are listed in the left-top corner of each panel.

(Iliadis 2015). To generate skeletal reactions, simulations are conducted of constant- ρT burning in SNe Ia for 24 cases, with $T_9 \in \{2, 4, 6\}, \, \rho_9 \in \{0.001, 0.01, 0.1, 1.0\}, \, \text{and} \, y_{e,0} \in \{0.4955, 0.5\}.$ To better show how these cases are distributed, a 2D version of Figure 5 is shown in Figure 6. Each case (shown as a red circle in Figure 6) denotes a set of initial condition for the density, the temperature, the energy, and isotope mass fractions. These conditions cover the burning stage, and are of interest in multidimensional simulations (Fryxell et al. 2000; Woosley et al. 2007).

The final time for each case is when the mass fraction of ⁵⁶Ni reaches its maximum. Figure 7 shows the evolution of isotope mass fractions for two different cases. The red lines in Figure 7

show the ⁵⁶Ni mass fraction and blue triangles denote the final time of f-OTD simulations and sensitivity analysis. The initial mass fractions of ¹²C, ¹⁶O, and ²²Ne isotopes in cases with $y_{e,0} = 0.5$ are $x_{C,0} = x_{O,0} = 0.5$, and in cases with $y_{e,0} = 0.4955$ are $x_{C,0} = 0.45$, $x_{O,0} = 0.45$, and $x_{Ne,0} = 0.1$. Note that for the conditions considered here, the sharp decline in ⁵⁶Ni mass fraction at $t \gtrsim 10$ s is likely due to electron capture, causing the network composition to shift to more neutron-rich isotopes of nickel and iron, which is not really relevant to carbon/oxygen burning and therefore not used in the f-OTD analysis. The f-OTD method is used to model the sensitivity matrix with an r = 1 mode, and the generated skeletal models by sensitivity analysis are denoted by f-OTD-n

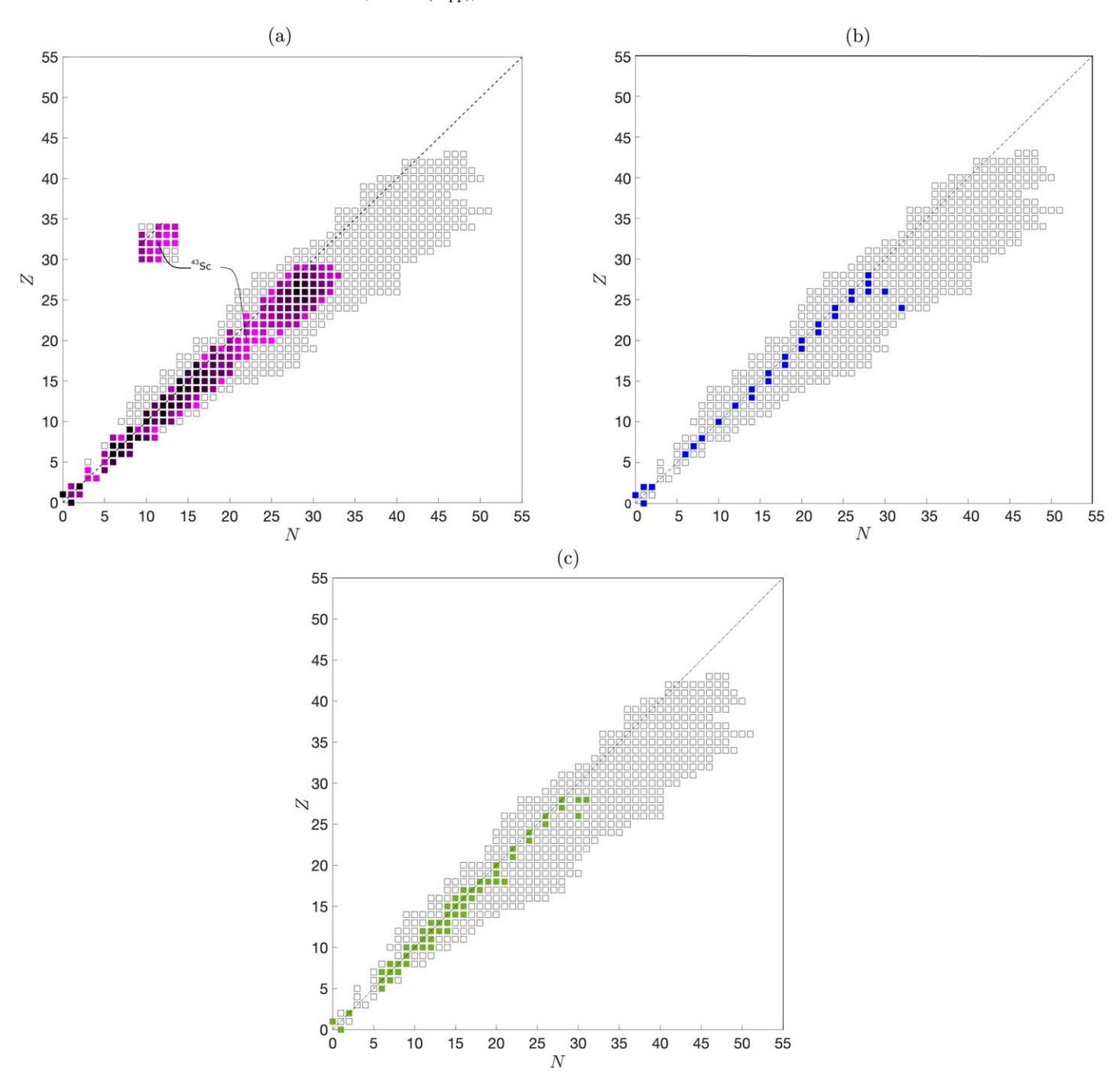


Figure 8. (a) The first 150 ranked isotopes of Torch RN sufficient for exact calculation of the maximum ⁵⁶Ni abundance and energy in SNe Ia. The darker the squares, the more important (higher-ranked) isotopes and the empty squares correspond to eliminated isotopes from the Torch RN. ⁴³Sc is a key isotope in proton and neutron channels toward ⁵⁶Ni production. The f-OTD models with less than 114 isotopes (Appendix) do not contain ⁴³Sc and do not produce the correct amount of ⁵⁶Ni. (b) The isotopes for Approx21 and (c) SK55.

in which "n" identifies for the number of isotopes. The predictive capabilities of f-OTD models are compared against those obtained via Torch RN and the Approx21.

A ranking is provided of the first 150 important isotopes in Table 1 in the Appendix considering the maximum characteristic value associated with each isotope, i.e., $w_{\max,i}$. Different skeletal models can be generated by applying a threshold ϵ on w_{\max} and eliminating isotopes and their associated reactions with $w_{\max,i} < \epsilon$ from Torch RN. A comprehensive skeletal model capable of reproducing the energy and isotope mass fraction predictions of Torch RN with a certain accuracy can be

developed by specifying an acceptable error level, e.g., 5%, in energy or 56 Ni mass fraction estimations. Figure 8(a) shows the isotopes in Torch selected for the f-OTD-150. Each square belongs to an isotope, and isotopes with darker colors are ranked higher (selected earlier) than isotopes with lighter colors. The results show at least 114 isotopes are required to accurately produce 56 Ni with a f-OTD skeletal model. This is because of the importance of some isotopes with $21 \le N$, $Z \le 24$, and especially 43 Sc in bridging between lighter and heavier isotopes and two quasistatic equilibrium clusters (Iliadis 2015; Subedi et al. 2020). It is shown in Figure 8(a) that 43 Sc plays a key role

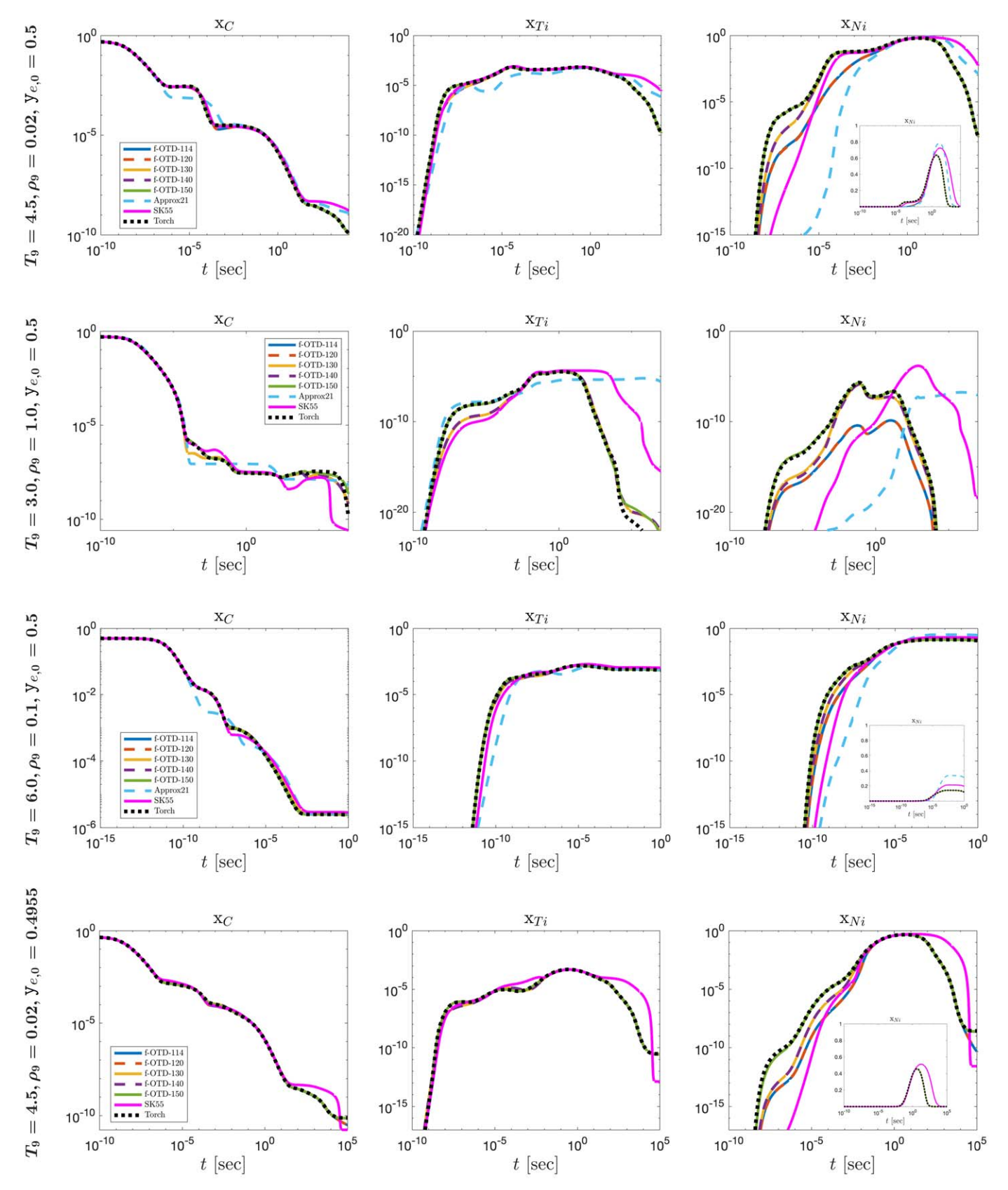


Figure 9. Model reduction on Torch RN: mass fraction estimations via Torch RN, Approx21, SK55, and f-OTD generated models for four different initial conditions of x_{c12} , x_{c16} , T_9 , and ρ_9 .

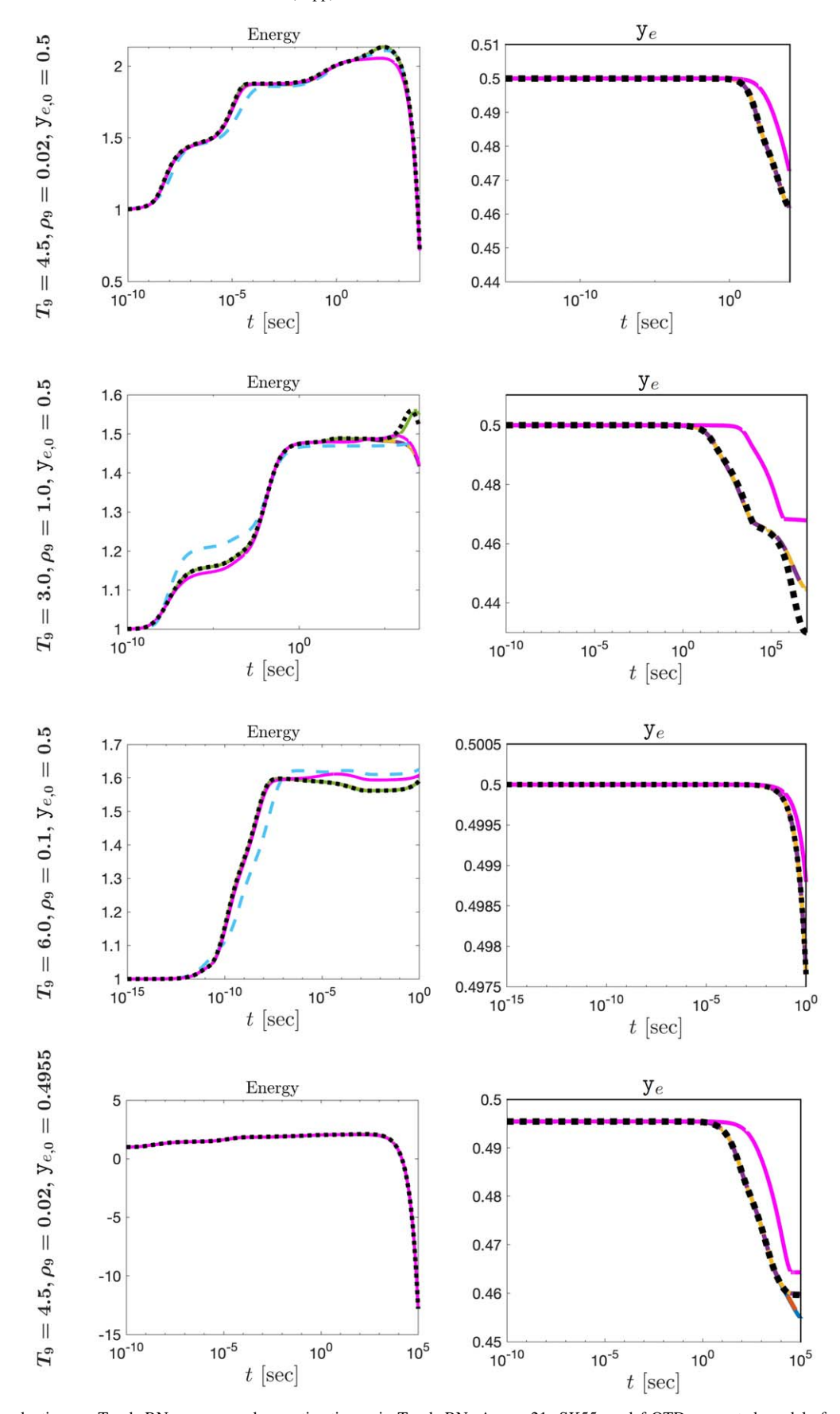


Figure 10. Model reduction on Torch RN: energy and y_e estimations via Torch RN, Approx21, SK55, and f-OTD generated models for four different initial conditions of x_{c12} , x_{c16} , T_{9} , and T_{9} .

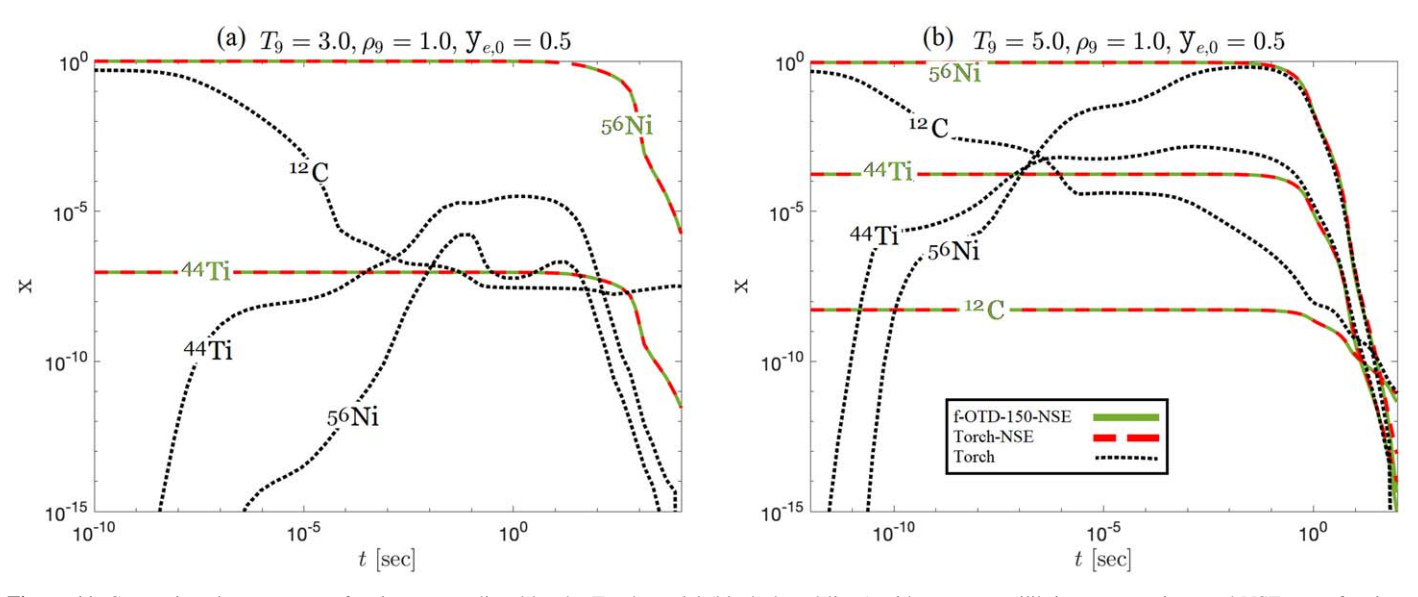


Figure 11. Comparison between mass fractions as predicted by the Torch model (black dotted lines) without any equilibrium assumptions and NSE mass fractions estimated based on Torch and f-OTD-150 models (green solid and red dashed lines). NSE and non-NSE simulations have same y_e at each time.

for proton and neutron channels. Figures 8(b) and (c) show the isotopes used in the Approx21 model and SK55, a skeletal model used by Townsley et al. (2019).

The Torch RN is user friendly and flexible to work with any subset of its own isotopes. This means that by providing a ranked list of isotopes from the Appendix, e.g., ¹⁶O (1st rank) to ⁴⁵Ca (150th rank), one can use an f-OTD generated network with the associated isotopes. Figures 9 and 10 show the performance of the f-OTD models in reproducing the energy and mass fractions of 12 C, 44 Ti, and 56 Ni, and y_e . The radioactive decays of 44 Ti and 56 Ni have significant observational applications, and the production of these two isotopes is sensitive to the temperature, density, and y_e evolution (Magkotsios et al. 2010). The energy in Figure 10 is normalized by its initial value. The predictions via the Approx21 and SK55 are also presented. The second and third rows of panels correspond to situations exactly similar to the test cases, but the first and last rows portray the estimations for arbitrary situations within the initial condition domain, i.e., $T_9 \in [2, 6]$, $\rho_9 \in [0.001, 1.0]$, and $y_{e,0} \in [0.4955, 0.5]$. It is apparent that the f-OTD models with $n_s \ge 150$ exactly predict the energy evolution of Torch RN and ⁵⁶Ni mass fraction within their designed ρ_9 – T_9 – Y_e ranges. The Approx21 and SK55 models usually overpredict the maximum 56 Ni mass fraction, and Approx21 cannot be used when $y_{e,0} \neq 0.5$. Replacing Torch with f-OTD models using 114-150 isotopes yields compression ratios ranging from 3.3 to 4.3. Figure 11 compares the evolution of mass fractions as predicted by the Torch model, without any approximation, and nuclear statistical equilibrium (NSE) assumption. The NSE results are generated by using the instantaneous values of ρ_9 – T_9 – Y_e extracted from non-NSE calculations. The Torch and f-OTD-150 are used as the base reaction network for NSE estimations. It is shown in Figures 11(a) and (b) that only at late time for $T_9 = 5$ are the NSE and non-NSE mass fraction predictions of ⁴⁴Ti and ⁵⁶Ni (but not ¹²C) close to each other.

5. Conclusions

A systematic method for skeletal model reduction of nuclear reaction networks is developed for generating models for the carbon–oxygen combustion in SNe Ia covering a range of temperatures and electron number fractions, $y_e = Z_m/A_m$. In

this method, the sensitivities of abundances with respect to reaction rates are modeled using the f-OTD method and are analyzed instantaneously. This results in reaction and isotope rankings based on the correlations between their sensitivities. A key feature of this approach is that it factorizes the sensitivity matrix into a multiplication of two low-ranked time-dependent matrices which evolve based on evolution equations derived from the governing equations of the system. The generated skeletal models are comparatively assessed based on their ability to predict the energy and mass fractions. In particular, the skeletal models as derived here are the first to address situations covering both $y_e = 0.5$ and $y_e < 0.5$. To employ any of the skeletal models developed in this work or to create new f-OTD skeletal models with different numbers of isotopes, one only needs to feed a list of more than 114 ranked isotopes from the Appendix into the Torch RN (see footnote 3). Further reduction in the number of isotopes (e.g., by using equilibrium assumptions) is a potential future follow-up to this work.

The overall costs of generating an f-OTD model depend on solving the mass fraction equations (which is roughly the same as one non-f-OTD Torch simulation, $c_{\rm torch}$), the U equation, whose cost scales as $r \times c_{\rm torch}$, and the V equation, whose cost scales as $r \times n_r/n_s \times c_{\rm torch}$. For example, the total cost to generate the f-OTD-150 model with r=1 modes, for which 10 cases with different densities and temperatures were used, was $\sim 120c_{\rm torch}$, which would be negligible, for example, compared to a Monte Carlo simulation with $\sim 10,000$ trials. On the other hand, f-OTD-150 should run ~ 3.3 faster than Torch.

The skeletal reduction technique as described here can be readily extended to other situations. For example, lower values of y_e and higher densities to examine the production of ⁴⁸Ca, ⁵⁰Ti, or ⁵⁴Cr. It can also be applied to more complex RNs to examine the production of heavier elements in core-collapse SNe. With respect to the development of the methodology itself, it can be extended by including the sensitivity analysis based also on transport properties, or even the equation of state (Nouri et al. 2019). Most importantly, as shown recently (Donello et al. 2022), the f-OTD methodology can be used for solving partial differential equations for multidimensional combustion problems in a cost-effective manner—by

exploiting the correlations between the spatiotemporal sensitivities of different species with respect to different parameters. This analysis can be especially insightful for problems containing rare events by providing more insights into global phenomena.

Acknowledgments

This article is coauthored by D.L., an employee of Triad National Security, LLC, which operates Los Alamos National Laboratory under Contract No. 89233218CNA000001 with the U.S. Department of Energy/National Nuclear Security Administration. The work at Pitt is supported by Los Alamos National Laboratory, under Contract 614709. Additional support for the work at Pitt is provided by NSF under grant CBET-2042918

and grant CBET-2152803. The authors are indebted to Prof. Frank Timmes for very useful suggestions on an earlier version of the manuscript.

$\label{eq:Appendix} Appendix \\ \mbox{Isotope Ranking Based on All Cases } (y_{e,0}\leqslant 0.5)$

Table 1 contains the ranking of the first 150 important isotopes of the Torch reaction network based on the maximum characteristic value associated with each isotope, i.e., $w_{\text{max},i}$. Different skeletal models can be generated by applying a threshold ϵ on bw_{max} and eliminating isotopes and their associated reactions with $w_{\text{max},i} < \epsilon$ from Torch RN.

 Table 1

 The First 150 Important Isotopes of Torch RN Ranked by f-OTD Analysis

Rank	Isotope	$w_{\rm max}$	Rank	Isotope	w _{max}	Rank	Isotope	$w_{\rm max}$	Rank	Isotope	w _{max}
1	¹⁶ O	0.967	41	³² P	0.112	81	²⁷ Mg	0.020	121	⁶¹ Ni	0.003
2	²⁰ Ne	0.967	42	35Cl	0.105	82	⁵⁰ V	0.018	122	⁴⁵ Sc	0.002
3	⁴ He	0.967	43	⁵² Cr	0.094	83	⁵⁴ Cr	0.018	123	⁴⁵ Ti	0.002
4	¹² C	0.935	44	⁵² Mn	0.094	84	³⁹ K	0.016	124	$^{40}{ m K}$	0.002
5	²³ Na	0.796	45	⁵⁶ Ni	0.094	85	²⁴ Na	0.014	125	⁵² V	0.002
6	р	0.796	46	³⁵ S	0.093	86	^{2}H	0.014	126	¹⁸ F	0.002
7	³¹ P	0.761	47	⁵⁷ Co	0.085	87	⁵⁹ Co	0.012	127	⁴⁴ Ti	0.002
8	²⁸ Si	0.743	48	⁵⁷ Ni	0.085	88	⁵⁹ Ni	0.012	128	⁵⁶ Mn	0.001
9	^{13}N	0.732	49	^{30}P	0.083	89	⁵³ Co	0.011	129	⁵⁸ Cu	0.001
10	⁵⁴ Fe	0.707	50	⁵¹ Cr	0.081	90	³⁸ Ar	0.011	130	⁷ Li	0.001
11	⁵⁵ Co	0.707	51	⁵¹ Mn	0.081	91	^{3}H	0.010	131	⁴¹ K	0.001
12	¹⁷ F	0.704	52	23 Mg	0.076	92	³ He	0.010	132	⁵⁵ Ni	0.001
13	^{29}P	0.681	53	²¹ Ne	0.075	93	¹¹ C	0.010	133	⁶ Li	0.001
14	24 Mg	0.669	54	^{18}O	0.066	94	⁴⁰ Ca	0.009	134	¹⁵ O	0.001
15	²⁵ Mg	0.669	55	³⁴ S	0.066	95	⁴¹ Sc	0.009	135	⁴⁰ Ar	0.001
16	n	0.669	56	⁵⁵ Mn	0.066	96	^{14}O	0.009	136	⁴⁷ Sc	0.001
17	¹³ C	0.667	57	⁹ Be	0.066	97	^{48}V	0.009	137	⁵⁰ Mn	0.001
18	^{14}N	0.624	58	¹⁴ C	0.061	98	⁴⁸ Cr	0.009	138	⁵¹ Fe	0.001
19	¹⁷ O	0.624	59	³⁶ Ar	0.052	99	⁴⁹ Ti	0.008	139	⁷ Be	0.001
20	³⁰ Si	0.518	60	³⁷ K	0.052	100	²⁹ Al	0.007	140	³⁵ Ar	0.001
21	³³ S	0.518	61	⁵⁷ Fe	0.052	101	⁵⁰ Ti	0.007	141	⁴³ Ca	0.001
22	²² Ne	0.447	62	⁵² Fe	0.051	102	⁴⁷ Ti	0.007	142	⁴⁴ Ca	0.001
23	^{32}S	0.441	63	²⁸ Al	0.048	103	⁴⁷ V	0.007	143	⁴⁴ Sc	0.001
24	³³ Cl	0.441	64	³⁷ Ar	0.046	104	⁴⁸ Ti	0.007	144	^{34}P	0.001
25	²⁵ Al	0.385	65	⁵⁰ Cr	0.044	105	²⁷ Si	0.006	145	^{38}K	0.001
26	⁵⁵ Fe	0.352	66	⁵⁸ Co	0.042	106	³⁹ Ar	0.006	146	⁴² Ca	0.001
27	²⁹ Si	0.330	67	⁵⁸ Ni	0.042	107	⁵⁴ Co	0.005	147	²⁰ F	0.001
28	¹¹ B	0.295	68	²³ Ne	0.042	108	⁶⁰ Cu	0.005	148	⁴⁵ V	0.001
29	¹⁵ N	0.285	69	⁵¹ V	0.040	109	³⁴ Cl	0.005	149	28 Mg	0.001
30	²¹ Na	0.264	70	³⁷ Cl	0.040	110	⁴⁹ Mn	0.005	150	⁴⁵ Ca	0.001
31	⁵⁴ Mn	0.191	71	²⁶ Al	0.038	111	⁵⁷ Cu	0.004			
32	²⁷ Al	0.177	72	²² Na	0.033	112	⁵⁸ Fe	0.004			
33	⁵⁶ Fe	0.163	73	⁴⁹ V	0.030	113	⁴⁶ Ti	0.004			
34	⁵⁶ Co	0.163	74	⁴⁹ Cr	0.030	114	⁴³ Sc	0.004			
35	26 Mg	0.161	75	⁵⁹ Cu	0.027	115	$^{10}\mathrm{B}$	0.004			
36	³³ P	0.155	76	⁵³ Cr	0.027	116	⁶⁰ Ni	0.003			
37	³¹ Si	0.142	77	¹⁹ F	0.025	117	⁶¹ Cu	0.003			
38	⁵³ Mn	0.128	78	³² Si	0.024	118	²⁵ Na	0.003			
39	⁵³ Fe	0.128	79	³⁶ S	0.022	119	¹⁹ O	0.003			
40	³¹ S	0.124	80	³⁶ Cl	0.022	120	⁴¹ Ca	0.003			

ORCID iDs

- A. G. Nouri https://orcid.org/0000-0001-7390-5212 Y. Liu https://orcid.org/0000-0001-5261-8994 P. Givi https://orcid.org/0000-0002-9557-5768
- H. Babaee https://orcid.org/0000-0002-6318-2265
- D. Livescu https://orcid.org/0000-0003-2367-1547

References

- Aitzhan, A., Nouri, A., Givi, P., & Babaee, H. 2022, arXiv:2201.02097 Anninos, P., Hoffman, R., Grewal, M., Lavell, M., & Fragile, P. 2019, ApJ,
- Arnett, W. D. 1996, Supernovae and Nucleosynthesis: An Investigation of the History of Matter, from the Big Bang to the Present (Princeton, NJ: Princeton Univ. Press)
- Arnould, M., & Goriely, S. 2020, PrPNP, 112, 103766
- Babaee, H. 2019, RSPSA, 475, 20190506
- Babaee, H., Choi, M., Sapsis, T., & Karniadakis, G. 2017a, JCoPh, 344, 303 Babaee, H., Farazmand, M., Haller, G., & Sapsis, T. P. 2017b, Chaos, 27,
- Barnes, J., Zhu, Y., Lund, K., et al. 2021, ApJ, 918, 44
- Beaudet, G., & Reeves, H. 1983, in ESO Workshop on Primordial Helium (Garching: European Southern Observatory), 53
- Bliss, J., Arcones, A., Montes, F., & Pereira, J. 2020, PhRvC, 101, 055807
- Bodansky, D., Clayton, D., & Fowler, W. 1968, ApJS, 16, 299
- Bora, Z., Vinkó, J., & Könyves-Tóth, R. 2022, PASP, 134, 054201
- Bravo, E., Badenes, C., & Martínez-Rodríguez, H. 2019, MNRAS, 482, 4346
- Bravo, E., & Martinez-Pinedo, G. 2012, PhRvC, 85, 055805
- Cheng, M., Hou, T., & Zhang, Z. 2013, JCoPh, 242, 843
- Cyburt, R. 2004, PhRvD, 70, 023505
- Delbourgo-Salvador, P., Gry, C., Malinie, G., & Audouze, J. 1985, A&A,
- Donello, M., Carpenter, M., & Babaee, H. 2022, SJSC, 44, A128
- Fernández, R., Foucart, F., Kasen, D., et al. 2017, CQGra, 34, 154001
- Fryxell, B., Olson, K., Ricker, P., et al. 2000, ApJS, 131, 273
- Fuller, G., Fowler, W., & Newman, M. 1985, ApJ, 293, 1
- Girimaji, S., & Ibrahim, A. 2014, J. Fluids Eng., 136, 031201
- Goussis, D. 2012, CTM, 16, 869
- Guidry, M., Budiardja, R., Feger, E., et al. 2013, CS&D, 6, 015001
- Guidry, M., & Harris, J. 2013, CS&D, 6, 015002
- Hadi, F., Janbozorgi, M., Sheikhi, M., & Metghalchi, H. 2016, JNET, 41, 257
- Hillebrandt, W., & Niemeyer, J. C. 2000, ARA&A, 38, 191
- Hix, W., Khokhlov, A., Wheeler, J., & Thielemann, F. 1998, ApJ, 503, 332 Hix, W., Parete-Koon, S., Freiburghaus, C., & Thielemann, F. 2007, ApJ,
- Hix, W., Smith, M., Starrfield, S., Mezzacappa, A., & Smith, D. 2003, NuPhA,
- Iliadis, C. 2015, Nuclear Physics of Stars (New York: Wiley)
- Johnson, J. 2019, Sci, 363, 474
- Keck, J. C. 1990, PECS, 16, 125
- Khokhlov, A. 1981, SvAL, 7, 410
- Kobayashi, C., Karakas, A., & Lugaro, M. 2020, ApJ, 900, 179
- Koch, O., & Lubich, C. 2007, SIAM J. Matrix Anal. Appl., 29, 434
- Krauss, L., & Romanelli, P. 1990, ApJ, 358, 47
- Kushnir, D., & Katz, B. 2020, MNRAS, 493, 5413
- Leung, S., & Nomoto, K. 2018, ApJ, 861, 143
- Li, Y., Chen, Y., & Wu, G. 2020, Fuel, 264, 116856
- Lippuner, J., & Roberts, L. 2017, ApJS, 233, 18

- Longland, R. 2012, A&A, 548, A30 Longland, R., Iliadis, C., Champagne, A., et al. 2010, NuPhA, 841, 1 Lu, T., & Law, C. 2009, PECS, 35, 192 Magkotsios, G., Timmes, F., Hungerford, A., et al. 2010, ApJS, 191, 66 Matteucci, F. 2012, Chemical Evolution of Galaxies (Berlin: Springer) Meyer, B., Krishnan, T., & Clayton, D. 1998, ApJ, 498, 808 Mott, D., Oran, E., & van Leer, B. 2000, JCoPh, 164, 407 Mumpower, M., McLaughlin, G., & Surman, R. 2012, PhRvC, 86, 035803 Mumpower, M., Surman, R., Fang, D., et al. 2015, PhRvC, 92, 035807
- Nishimura, N., Takiwaki, T., & Thielemann, F. 2015, ApJ, 810, 109
- Nollett, K., & Burles, S. 2000, PhRvD, 61, 123505
- Nomoto, K. 1997, Sci, 276, 1378
- Nouri, A., Babaee, H., Givi, P., Chelliah, H., & Livescu, D. 2022, CoFl, 235,
- Nouri, A., Givi, P., & Livescu, D. 2019, PrAeS, 108, 156

Liu, Y., Babaee, H., Givi, P., et al. 2024, Fuel, 357, 129581

- Pagel, B. 2009, Nucleosynthesis and Chemical Evolution of Galaxies (Cambridge: Cambridge Univ. Press)
- Parikh, A., José, J., Moreno, F., & Iliadis, C. 2008, ApJS, 178, 110
- Patil, P., & Babaee, H. 2020, JCoPh, 415, 109511
- Paxton, B., Bildsten, L., Dotter, A., et al. 2011, ApJS, 192, 3
- Paxton, B., Marchant, P., Schwab, J., et al. 2015, ApJS, 220, 15
- Peters, N., & Rogg, B. (ed.) 1993, Reduced Kinetic Mechanisms for Applications in Combustion Systems (Berlin: Springer)
- Psaltis, A., Arcones, A., Montes, F., et al. 2022, ApJ, 935, 27
- Ramezanian, D., Nouri, A., & Babaee, H. 2021, CMAME, 382, 113882
- Rein, M. 1992, PhFIA, 4, 873
- Röpke, F., & Sim, S. 2018, SSRv, 214, 72
- Sapsis, T., & Lermusiaux, P. 2009, PhyD, 238, 2347
- Seitenzahl, I., & Pakmor, R. 2023, in Handbook of Nuclear Physics, ed. I. Tanihata et al. (Singapore: Springer), 3809
- Seitenzahl, I., & Townsley, D. 2017, in Handbook of Supernovae, ed. A. W. Alsabti & P. Murdin (Cham: Springer), 1955
- Sieverding, A., Waldrop, P., Harris, J. A., et al. 2023, ApJ, 950, 27
- Smith, M., Kawano, L., & Malaney, R. 1993, ApJS, 85, 219 Smooke, M. D. 1991, Reduced Kinetic Mechanisms and Asymptotic Approximations for Methane-Air Flames: A Topical Volume (Berlin: Springer)
- Sprouse, T., Perez, R., Surman, R., et al. 2020, PhRvC, 101, 055803
- Stagni, A., Frassoldati, A., Cuoci, A., Faravelli, T., & Ranzi, E. 2016, CoFl, 163, 382
- Stiefenhofer, M. 1998, J. Math. Biol., 36, 593
- Subedi, S., Meisel, Z., & Merz, G. 2020, ApJ, 898, 5
- Thielemann, F. K., Nomoto, K., & Yokoi, K. 1986, A&A, 158, 17
- Timmes, F. X. 1999, ApJS, 124, 241
- Timmes, F. X., & Arnett, D. 1999, ApJS, 125, 277
- Timmes, F. X., Hoffman, R. D., & Woosley, S. E. 2000, ApJS, 129, 377
- Timmes, F. X., & Swesty, F. D. 2000, ApJS, 126, 501
- Townsley, D., Miles, B., Shen, K., & Kasen, D. 2019, ApJL, 878, L38
- Townsley, D., Miles, B., Timmes, F., Calder, A., & Brown, E. 2016, ApJS, 225, 3
- Wanajo, S. 2013, ApJL, 770, L22
- Weaver, T. A., Zimmerman, G. B., & Woosley, S. E. 1978, ApJ, 225, 1021
- Williams, F. A. 1985, Combustion Theory (2nd ed.; Menlo Park, CA: The Benjamin/Cummings Publishing Company)
- Woosley, S. 1997, ApJ, 476, 801 Woosley, S., Arnett, W., & Clayton, D. 1973, ApJS, 26, 231
- Woosley, S., Heger, A., & Weaver, T. 2002, RvMP, 74, 1015
- Woosley, S. E., Almgren, A., Bell, J. B., et al. 2007, JPhCS, 78, 012081
- Yoshida, T., Takiwaki, T., Kotake, K., et al. 2021, ApJ, 908, 44